Tribological behavior of Ti-Al-Si-C-N hard coatings deposited by hybrid arc-enhanced magnetron sputtering

Guizhi Wu, Shengli Ma,[a] and Kewei Xu
State Key Laboratory for Mechanical Behavior of Materials, Xi'an Jiaotong University, Xi'an 710049, China

Paul K Chu
Department of Physics and Materials Science, City University of Hong Kong, 83 Tat Chee Avenue, Kowloon, China

(Received 31 August 2011; accepted 17 December 2011; published 11 January 2012)

Ti-Al-Si-C-N hard coatings are deposited on high speed steel by hybrid arc-enhanced magnetron sputtering, and the hardness, adhesion, and tribological behavior are studied. On account of the nanocomposite structure, the coatings possess hardness of more than 30 GPa. Failure of the coating during the scratch test is due to the buckling and wedge spallation failure mechanism. Compared to Ti-Al-Si-N, the presence of C in the Ti-Al-Si-C-N coatings leads to reduced friction coefficient and wear rate, indicating effective lubrication rendered by amorphous C. According to the wear tracks examined by scanning electron microscopy, the wear mechanism can be explained by plowing abrasion. © *2012 American Vacuum Society*. [DOI: 10.1116/1.3676186]

I. INTRODUCTION

TiN-based coatings incorporated with other elements exhibit a wide variety of properties. For example, TiCN coatings have smaller friction coefficients than TiN,[1] and TiSiN coatings possess super high hardness of more than 40 GPa.[2,3] Owing to the fast development in high-speed cutting technology, cutting tools need to possess excellent oxidation resistance and hence, TiAlN coatings are popular in the cutting industry as they offer both higher hardness and superior oxidation resistance. It has been shown that the protective aluminum oxide layers are formed on TiAlN coating as a result of diffusion of Al atoms to the surface region, and the oxide layers prevent further oxidation.[4,5] Unfortunately, TiAlN coatings have large friction and so improvement is required.[6,7] One way to reduce friction during the machining process is the use of lubricants. However, lubricants are usually not environmentally friendly and some are toxic or flammable and pose health hazards.[8] Another means to reduce surface friction is to using hard coatings with better self-lubrication capability.[8–12] Self-lubricating coatings are coatings which exhibit reduced wear and friction without the need of using tribological fluids. The coatings serve as a reservoir of nanoparticles which are slowly released from the surface and provide easy shear and reduced oxidation of the coating.[13] TiCN, TiSiCN, TiBCN, etc. are TiN-based hard coatings.[14] C element is used to improve tribological property due to that carbon acts as lubricant decreasing friction and wear. In this study, new quintuple Ti-Al-Si-C-N hard coatings with different C contents are produced to improve the surface friction as well as wear resistance and the results are compared to those obtained from quarternary Ti-Al-Si-N coatings.

II. EXPERIMENTAL DETAILS

The Ti-Al-Si-C-N and Ti-Al-Si-N hard coatings with the same thickness of around 3.5 μm were deposited on W18Cr4V high speed steel (HSS) substrates by hybrid arc-enhanced magnetron sputtering (AEMS). A detailed description of the system can be found elsewhere.[15,16] Succinctly speaking, the apparatus consists of three pairs of dual magnetron targets and a titanium arc target. The titanium arc target was used to increase the plasma density and to enhance the adhesion between the coating and substrate. Prior to deposition, the HSS substrates were polished and cleaned with acetone and alcohol, followed by Ar ion sputtering. The coatings were synthesized by a pulsed dc bias voltage of -100 V, which the pulse frequency is 40KHz, substrate temperature of 200 °C and pressure of 0.3 Pa using a mixture of Ar_2 and N_2 (with a flow rate of 30 and 28 SCCM, respectively). The deposition time was 140 mins. The power applied to the Al target (5 kW) and Si target (3 kW) as well as the current of the Ti arc ion target (60 A) were kept constant and only the C target power was varied from 0 to 10 kW. In order to enhance the adhesion between the coating and substrate, a TiN interfacial layer with a thickness of $\sim$100 nm was first deposited on the substrate. This interlayer has been proven to be effective in improving the adhesion of coatings on steel substrates.[17,18] The composition of the coatings were determined by energy dispersive x-ray spectrometry (EDS) using an Oxford INCA Energy detector.

The microstructure and phase composition of coatings were investigated by x-ray diffraction (XRD), high-resolution transmission electron microscopy (HRTEM) using the Rigaku D/max-3 C diffractometer and JEM 2100F transmission electron microscope, respectively. The binding energy was determined by x-ray photoelectron spectroscopy (XPS) on the PHI 5802.

Vickers microhardness measurements were performed on a HV-1000 micro hardness tester equipped with a Vickers diamond indenter. The applied load was 0.2 N (20 gf) in order to keep the indentation depth below 1/10 of the coating thickness. The measurement error of the hardness test was about 10%.

The adhesion strength was evaluated by scratch measurements conducted on a WS-type scratch tester with a detector

[a]Electronic mail: slma@mail.xjtu.edu.cn

for acoustic emission. A Rockwell C diamond indenter (tip radius = 200 μm and angle of spherical head = 120°)[19] and a scratch speed of 60 N/min were adopted. The maximum load was 100 N. The critical loads leading to adhesive failure were determined by the change in the acoustic emission-normal load curve as well as scanning electron microscopy.

The friction coefficients and wear behavior were evaluated using a pin-on-disc tribometer at a load of 3.25 N. GCr15 bearing steel balls (3 mm diameter) were used as the counterparts. The tests were conducted at a sliding speed of 0.3 m/s at 28 °C and 45% relative humidity in air without lubricants and the sliding time was 60 min. The friction coefficients were determined as a function of sliding time. The surface morphology after the wear tests was examined by scanning electron microscopy (SEM, JSM 7000 F). The composition of the wear zone was determined by energy dispersive x-ray spectrometry (EDS) using an Oxford INCA Energy detector installed on the JSM 7000 F SEM. A Taylor Hobson profilometer (Talysurf series 2) was employed to scan the wear track to determine the wear volume.

III. RESULTS AND DISCUSSION

Table I lists the composition of the Ti-Al-Si-C-N coatings deposited with different power applied to the C target (0 kW to 10 kW) as well as the Ti-Al-Si-N coating without carbon. In order to simplify the nomenclature, only the content of C is marked. The C contents increase from 0 at % to 32 at % and N contents decrease from 48 at % to 28 at % as the C target power increases from 0 to 10 kW, whereas the Ti, Al and Si contents are around 18 at %, 14 at %, and 10 at %, respectively, except the Ti-Al-Si-N coating. As the C target power increases, more and more N atoms in coatings would probably be replaced by C atoms.[15,16] However, there is no evident correlation between the contents of Ti, Al and Si with C target powers.

Figure 1 shows the hardness of the Ti-Al-Si-C-N coatings. $TiAlSiC_{22}N$ coating possesses the highest hardness value of 39 GPa and the coating hardness is more than 35 GPa when the C content is below 22 at %. However, the hardness of the $TiAlSiC_{32}N$ coating decreases to 31 GPa when the C content is increased to 32 at %. Hence, a larger content of amorphous C reduces the hardness and consequently, the microstructure and phase composition of the coatings are further investigated.

Figure 2(a) presents the HR-TEM micrographs of the $TiAlSiC_{22}N$ coating together with the selected area electron

TABLE I. Composition of Ti-Al-Si-C-N coatings and the power applied to the C target.

Coating type	Ti (at%)	Al (at%)	Si (at%)	C (at%)	N (at%)	Power of C target (kW)
$TiAlSiC_{32}N$	17	14	9	32	28	10.0
$TiAlSiC_{22}N$	18	12	12	22	36	6.0
$TiAlSiC_{14}N$	18	14	11	14	43	3.5
$TiAlSiC_{7}N$	19	15	10	7	49	2.0
$TiAlSiC_{0}N$	25	16	11	0	48	0

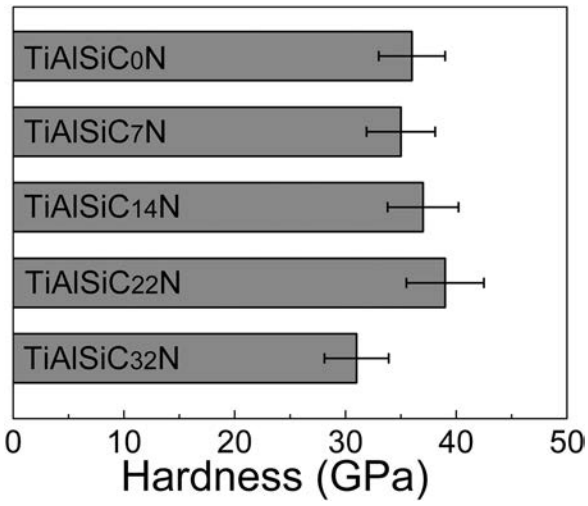

FIG. 1. Micro-hardness values of the Ti-Al-Si-C-N coatings at an applied load of 0.2 N.

diffraction pattern (SAED) shown on the left corner. The lattice parameter was calculated using SAED spectroscopy patterns in the figure. Since the diffraction rings are not sharp enough, the calculated value of d-spacing are in a range. Take the example of (200) orientation, the calculated values in Fig. 2(a) are in a range of 2.05–2.17, while the standard d-spacing of TiN (200), TiC (200), and AlN (200) is 2.12, 2.16, and 2.06, respectively. It appears that the Ti-Al-Si-C-N coatings should be a composite consisting of TiN, TiC, and AlN nanocrystallines. One can conclude that the coatings are probably composed of nanocrystallines of (Ti,Al)(C,N). The HR-TEM micrographs reveal a nanocomposite structure with the nanocrystallites embedded in the amorphous phase. Figure 2(b) shows the XRD patterns of the Ti-Al-Si-C-N coatings with different C concentrations, and the standard peaks of TiN, TiC, AlN, and Fe are labeled. The broad peak at around 35° suggests the presence of nanocrystalline phases in the coatings and the results are consistent with the HR-TEM image in Fig. 2(a). The microstructure of Ti-Al-Si-C-N coatings have been described in details[16] and the crystalline phase is found to be nanocrystalline (Ti,Al)(C,N). The phase composition revealed by the SAED pattern in Fig. 2(a) also supports this conclusion. Figure 2(c) shows the C1s XPS spectra of the Ti-Al-Si-C-N coatings with different C contents. The C-Ti peak and C-C peak are at approximately 281.6 eV and 284.3 eV, respectively. Besides the nanocrystallites (Ti,Al)(C,N), C exists as amorphous carbon since no carbon crystalline phase can be observed from Figs. 2(a) and 2(b). The C-C peak intensity increases with increasing C concentration, implying that the percentage of a-C increases with C concentration. According to Fig. 2 and Refs. 9 and 16, it can be concluded that the Ti-Al-Si-C-N coatings have a nanocomposite structure of nanocrystalline-(Ti,Al)(C,N)/amorphous-Si_3N_4/amorphous-C (i.e., nc-(Ti,Al)(C,N)/a-Si_3N_4/a-C).

Figure 3 depicts the schematic diagram illustrating the microstructural evolution of the Ti-Al-Si-C-N coatings with increasing C concentration. At first, it should be noticed that we just want to illustrate that there is a-C existing in coatings in Fig. 3, not to illustrate that a-C form grains or grainlike

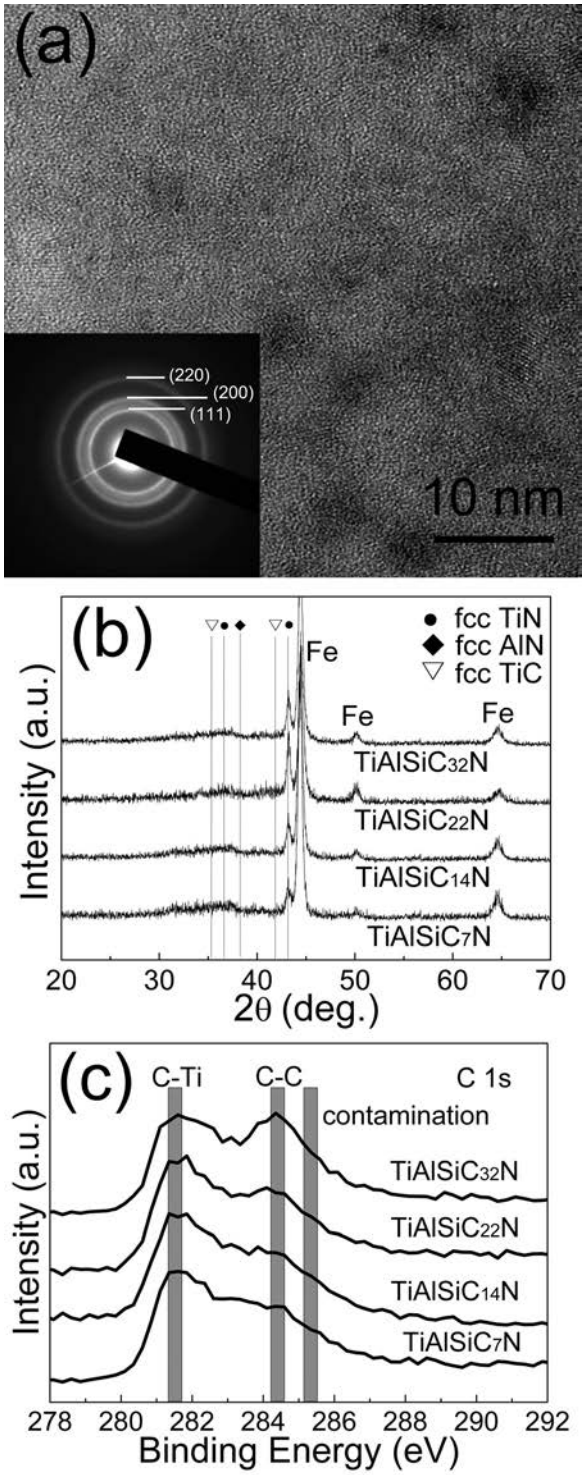

FIG. 2. (a) HR-TEM micrographs of the $TiAlSiC_{22}N$ coating together with the SAED patterns at the left corner; (b) XRD patterns of the Ti-Al-Si-C-N coatings with different C contents (the standard peaks positions of TiN, TiC, AlN as well as Fe are labeled); (c) C1s XPS spectra of the Ti-Al-Si-C-N coatings with different C contents.

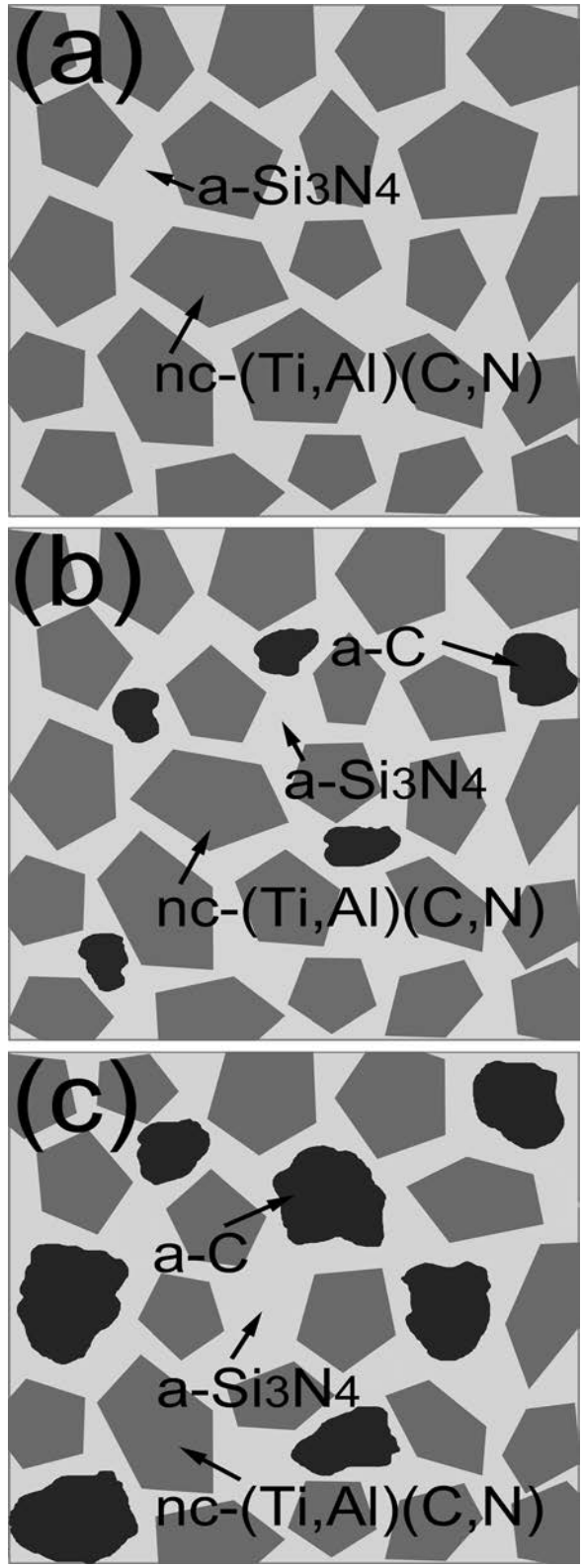

FIG. 3. Schematic diagram showing the microstructural evolution of the Ti-Al-Si-C-N coatings with increasing C concentrations with a-C, a-Si_3N_4, nc-(Ti,Al)(C,N) denoting amorphous C, amorphous Si_3N_4, and nanocrystalline (Ti,Al)(C,N), respectively.

structures. Figure 3(a) shows the typical nanocomposite structure without a-C (e.g., nc-(Ti,Al)(C,N)/a-Si_3N_4) and Fig. 3(b) shows the nanocomposite structure with a-C (e.g., nc-(Ti,Al)(C,N)/a-Si_3N_4/a-C). Although a-C exists in the nanocomposite matrix in Fig. 3(b), the coating hardness is still high as shown in Fig. 1. It is possibly due to the volume fraction of a-C being not sufficient to influence the nanocomposite structure and so the hardness does not decrease. However, as shown in Fig. 3(c), when the C content is increased furthermore, the volume fraction of a-C increases and the

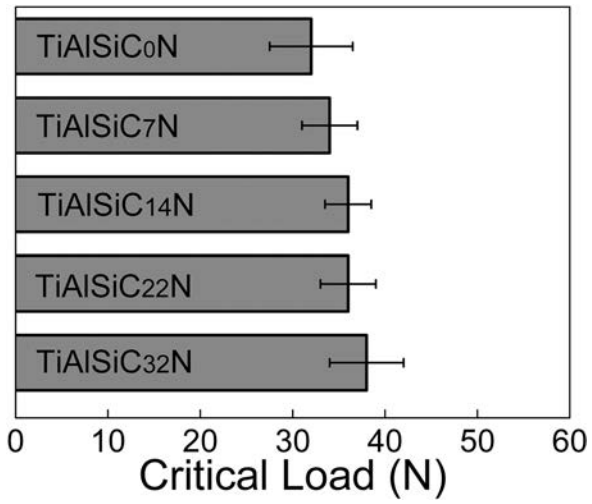

FIG. 4. Adhesion critical loads of the Ti-Al-Si-C-N coatings.

growth of crystallites are restrained. The inter-particle spacing of nanocrystallites also increases; thus decreasing the cohesive energy of the interface boundaries between the nanocrystallites and amorphous phases. This also contributes to the reduced coating hardness to 31 GPa for $TiAlSiC_{32}N$.

The adhesion critical loads of the Ti-Al-Si-C-N coatings are shown in Fig. 4 in. which $TiAlSiC_{32}N$ exhibits the highest critical load value of 38 N. The evolution of the nanocomposite structure may influence the adhesion property in such a way that with increasing volume fraction of the amorphous phase in the nanocomposite structure as show in Fig. 3, it is easier to relax the stress via plastic deformation during scratching. In this case, it is more difficult to form a crack and make it propagating. Therefore, a larger volume fraction of amorphous C enhances the adhesion property of the Ti-Al-Si-C-N coatings.

The critical loads for adhesive failure are determined by SEM. Fig. 5 shows the coating failure process in $TiAlSiC_{22}N$ after scratching. As indicated by Fig. 5(e), the first failure occurs at around 40 N, which is consistent with the critical value shown in Fig. 4. The results show that the failure mechanism of the other samples is similar to that of $TiAlSiC_{22}N$. In order to elucidate the failure mode of this coating, higher magnification images of different parts [parts (b), (c) and (d) in Fig. 5(a)] of the scratched track are shown in Figs. 5(b)–5(d), respectively. Figure 5(b) does not reveal evident failure despite small cracks on the edge of the track. A higher magnification image of the black rectangle area is shown at the right corner of Fig. 5(b) and cracks with an average length of about 20 μm can be seen. These cracks which are considered to be the failure mode of through-thickness cracking[20] may extend into the substrate and may stop at the interface. Figure 5(c) discloses a failure mode of coating detachment via the buckling failure mechanism and wedge spallation failure mechanism. Briefly speaking, failure occurs in response to the compressive stress generated ahead of the moving indenter. The localized regions containing interfacial defects allow the coating to buckle in response to the stress and individual buckles then spread laterally by

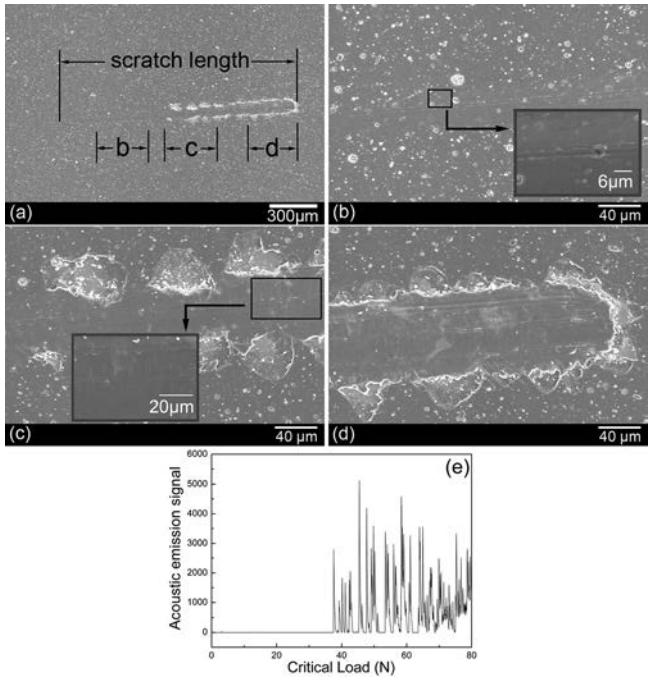

FIG. 5. Coating failure after the scratch test on $TiAlSiC_{22}N$ (scratch direction: from left to right); (a) entire scratch track, (b)-(d) higher magnification images of different parts of the scratch track in Fig. 6(a) showing the scratch failure mode, (e) critical load pattern of $TiAlSiC_{22}N$ coating.

propagation of an interfacial crack. Spallation occurs when through-thickness cracks form in regions of high tensile stress in the coating.[20] The left corner of Fig. 5(c) shows a higher magnification image of the black rectangle area and buckles can be readily observed. The buckles form in this region of plastic pile-up ahead of the moving indenter. The size of the buckle is less than 40 μm that is also less than the width of the track, implying that the pile-up process dominates the buckle failure mode.

As shown in Figs. 5(c) and 5(d), the fractures exhibit a fish scale shape. Initially, compressive shear cracks form at a distance and thickness ahead of the indenter and propagate to the surface and interface and generally have sloping sides which can act like a wedge. The continuing forward motion of the indenter drives the coating up the wedge causing the interfacial crack to propagate.[20] As the extent of interfacial failure increases, the wedge lifts the coating further away from the substrate and large enough displacements will cause a region ahead of the indenter to be detached. As a result, near the edge of the track, the coating is broken into relatively large pieces.

Figure 6 displays the friction coefficients curves of the Ti-Ai-Si-C-N coatings. All the curves exhibit two stages, namely the running-in stage and steady-state stage. In the running-in stage, the friction coefficient varies with sliding time whereas in the steady-state stage, the curves are smooth and constant. The sliding time at the running-in stage is less than 10 mins and in the steady-state stage, the friction curves are normally flat. As the C content is increased from 0 at % (TiAlSiN) to 32 at %, the average friction coefficient decreases from 0.7 to 0.25 and it is related to self-lubrication offered by the amorphous C.[8,9]

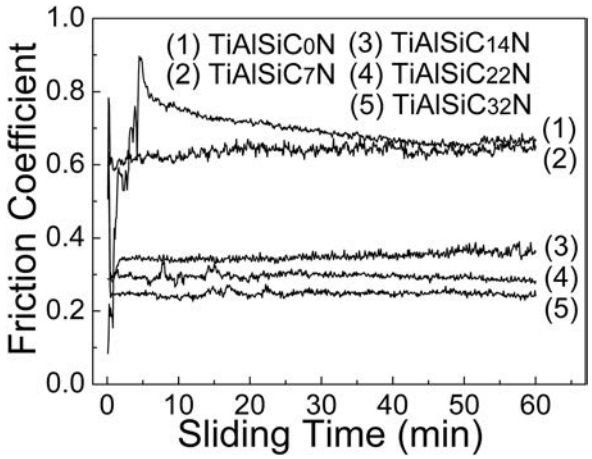

FIG. 6. Friction coefficients curves of the Ti-Al-Si-C-N coatings at a normal load of 3.25 N.

Figure 7 shows the volume wear rate of the Ti-Al-Si-C-N coatings. The wear rate is calculated by:[21,22]

$$Wv = \frac{V}{L \cdot S}, \tag{1}$$

where V is the wear volume (m^3), L is the applied load (N), and S is the sliding distance (m). The wear volume can be determined from the wear track profile.

The depths of the wear tracks are below 1.5 μm in all the coatings and less than the thickness of all coatings, indicating that no coating has been punched through. Figure 7 shows that the wear rate of Ti-Al-Si-N is 2.5×10^{-6} mm^3/Nm. As the C content is increased, the wear rate decreases and TiAlSiC$_{32}$N exhibits the smallest rate of 8.5×10^{-8} mm^3/Nm. It is because the amorphous C acts as a lubricating medium during the sliding test.

The wear tracks of the Ti-Al-Si-C-N coatings are shown in Fig. 8. The elemental contents of the wear tracks determined by EDS are shown at the right corner of each graph. Besides Ti, Al, Si, C, and N, other elements such as O, Fe, and Cr are also revealed by Figs. 8(b)–8(e). Some of the Fe and Cr originate from debris particles stripped from the counterpart ball. During the wear test, the counterpart ball and coating move against each other and heat is generated. As the temperature rises, oxidation become more likely and it explains the presence of O in the wear track. According to Fig. 8(a), O is hardly detected from the wear track possibly due to the good lubricating effect rendered by a-C. As shown in Fig. 6, TiAlSiC$_{32}$N has the smallest average friction coefficient of about 0.25. Therefore, low friction can effectively reduce the contact temperature during dry sliding and reduce the thermal load.

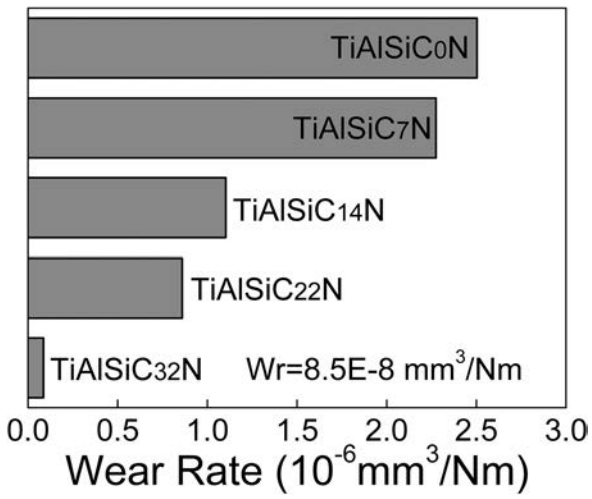

FIG. 7. Wear rates of various Ti-Al-Si-C-N coatings with TiAlSiC$_{32}$N showing the smallest wear rate of about 8.5×10^{-8} mm^3/Nm.

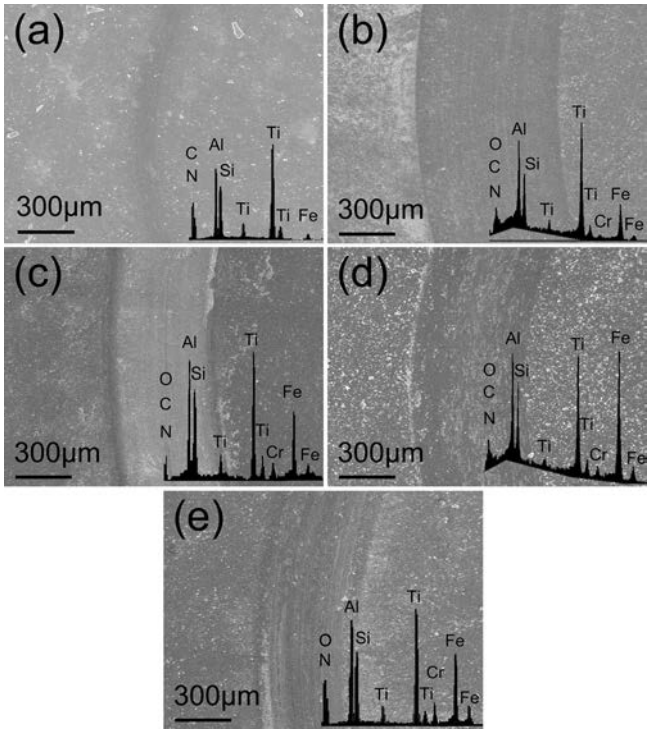

FIG. 8. Micrographs of wear tracks: (a) TiAlSiC$_{32}$N, (b) TiAlSiC$_{22}$N, (c) TiAlSiC$_{14}$N, (d) TiAlSiC$_7$N, and (e) TiAlSiC$_0$N with the EDS results shown at the right corner of each graph.

The width of the wear track shown in Fig. 8(a) is about 150 μm which is less than those of other samples. Moreover, the wear track on TiAlSiC$_{32}$N is smooth as shown in Fig. 9(a), suggesting excellent wear resistance which is consistent with the coating wear rate. The width of the wear tracks on other coatings is more than 600 μm. Although the width of the wear track on TiAlSiC$_{22}$N is about 900 μm as shwon in Fig. 8(b), this coating shows a smaller wear rate as shown in Fig. 7. It can be ascribed to the effect that the highest hardness of TiAlSiC$_{22}$N shown in Fig. 1 leads to better wear resistance.

During the sliding test, the wear interface generates high contact stress and high temperature possibly leading to adhesion wear. As shown in Figs. 8(d), 8(e), 9(d), and 10(e), many wear debris exist on the wear track surface of TiAlSiC$_0$N and TiAlSiC$_7$N, indicating that the failure mechanism is adhesion wear. When the C content is increased, grooves appear and dominate in the wear track as shown in Figs. 8(b), 8(c), 9(b), and 9(c). The lubrication effect of a-C should reduce adhesion

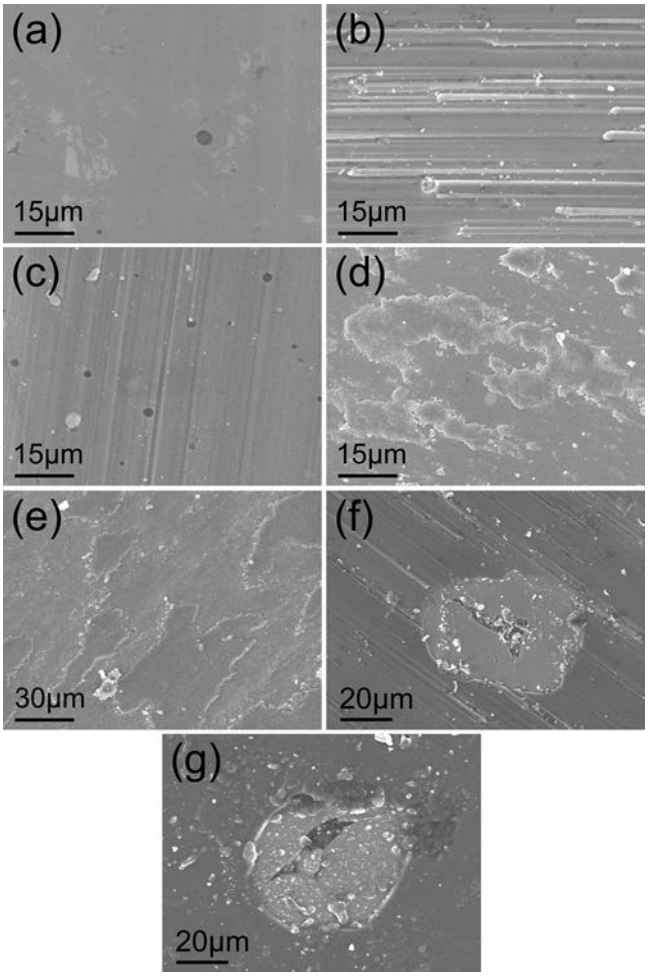

FIG. 9. Micrographs of the wear tracks revealing the failure modes: (a) $TiAlSiC_{32}N$, (b) $TiAlSiC_{22}N$, (c) $TiAlSiC_{14}N$, (d) $TiAlSiC_7N$, (e) $TiAlSiC_0N$, (f) $TiAlSiC_{22}N$ delaminating from the substrate, and (g) $TiAlSiC_7N$ peeling off from the substrate.

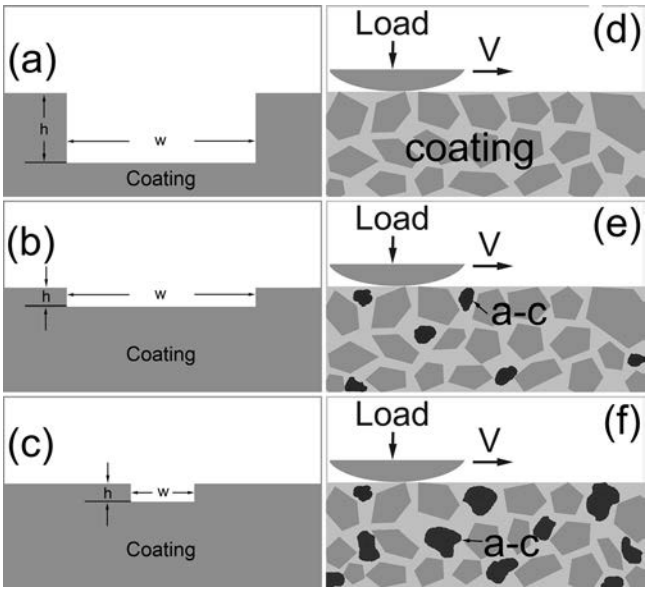

FIG. 10. Schematic diagrams of the cross-sectional wear tracks and related Ti-Al-Si-C-N coating phase structure: (a), (d) without a-C; (b), (e) small a-C content; (c), (f) large a-C content.

wear and abrasion is mainly due to plowing abrasion. However, the volume wear rates of $TiAlSiC_{14}N$ and $TiAlSiC_{22}N$ are still small as shown in Fig. 7. The high hardness should result in better wear resistance. As shown in Fig. 9(a), the wear track is smooth and no evident plowing grooves and abrasion debris can be seen. Hence, it can be concluded that a-C plays a very important role in reducing friction and abrasion, and the wear mechanism of Ti-Al-Si-C-N is mainly adhesion abrasion and plowing abrasion. Figs. 9(f) and 9(g) reveal unusual failure manifested as delamination from $TiAlSiC_{22}N$ and $TiAlSiC_7N$. This type of failure may be due to the high contact stress of the wear interface and fatigue failure from cyclic stress. It should be noted that this type of failure cannot be observed from the other coatings.

Figure 10 shows the schematic diagrams of cross-sectional wear tracks and according to Figs. 10(a)–10(c), the C content of the coating increases. Meanwhile, the schematic diagrams of the coating phase structure associated with Figs. 10(a)–10(c) are shown in Figs. 10(d)–10(f), respectively. As shown in Figs. 10(a) and 10(d), the wear track is the deepest and widest due to the absence of a-C in the coating. On the contrary, as shown in Figs. 10(c) and 10(f), the wear track is shallow and narrow as benefited by the large a-C volume fraction. During the wear test, heat is generated thereby making the contact area to be more easily worn. If a-C exists in the coating, it plays a lubricating role and decreases the contact area between the counterpart ball and coating. In this case, only slight wear should result, but on the contrary, if there is no a-C, the coating should experience extensive wear and tear. As shown in Fig. 4, a larger content of a-C makes it easier to relax the stress via plastic deformation and it is more difficult for the cracks to form and propagate. As a result, Fig. 10(c) exhibits the smallest wear volume.

It is thought that during wear test, the a-C was "released" from the coating. On account of the high contact temperature during the dry sliding test, plastic deformation occurs in the coating and the a-C migrates gradually to the surface to play the sustaining lubricating role as long as the coating is not wear through.

IV. CONCLUSION

Ti-Al-Si-C-N hard coatings boasting a surface hardness of more than 30 GPa are prepared by hybrid arc-enhanced magnetron sputtering. Compared to the Ti-Al-Si-N coatings, the tribological behavior of the Ti-Al-Si-C-N coatings is improved. Both the friction coefficients and wear rates decrease as the C concentration increases. It is because the a-C phase produces the lubricating effect reducing both the friction and wear. The wear mechanism of the Ti-Al-Si-C-N coatings as inferred from the wear tracks is mainly adhesion and plowing abrasion. It arises from the high contact stress at the wear interface and fatigue failure resulting from cyclic stress.

ACKNOWLEDGMENTS

This work was supported by the International Science and Technology Cooperation Program of China (Grant No.

2008DFA51470) and Hong Kong Research Grants Council (RGC) General Research Funds (GRF) Grant No. CityU 112510.

[1]Y. H. Cheng, T. Brown, and B. Heckerman, J. Vac. Sci. Technol. A. **28**, 431 (2010).
[2]Y. H. Cheng, T. Browne, B. Heckerman, and E. I. Meletis, Surf. Coat. Technol. **204**, 2123 (2010).
[3]S. Veprek, R. F. Zhang, M.G.J. Veprek-Heijman, S. H. Sheng, and A. S. Argon, Surf. Coat. Technol. **204**, 1898 (2010).
[4]F. Vaz, L. Rebouta, M. Andritschky, M. F. da Silva, and J. C. Soares, J. Euro. Ceram. Soc. **17**, 1971 (1997).
[5]F. Vaz, L. Rebouta, M. Andritschky, M. F. da Silva, and J. C. Soares, Surf. Coat. Technol. **9**, 912 (1998).
[6]S. PalDey and S. C. Deevi, Mater. Sci. Eng. A. **342**, 58 (2003).
[7]W. D. Munz, J. Vac. Sci. Technol. A. **4**, 2717 (1986).
[8]S. L. Ma, D. Y. Ma, Y. Guo, B. Xu, G. Z. Wu, K. W. Xu, and P. K. Chu, Acta Mater. **55**, 6350 (2007).
[9]D. V. Shtansky, P. V. Kiryukhantsev-Korneev, A. N. Sheveyko, B. N. Mavrin, C. Rojas, A. Fernandez, and E. A. Levashov, Surf. Coat. Technol. **203**, 3595 (2009).
[10]Y. Z. Huang, M. Streber, and P. Hovsepian, Appl. Surf. Sci. **253**, 2470 (2006).
[11]A. Erdemir, Surf. Coat. Technol. **200**, 1792 (2005).
[12]K. Kutschej, P. H. Mayrhofer, M. Kathrein, P. Polcik, C. Mitterer, Surf. Coat. Technol. **188–189**, 358 (2004).
[13]L. Rapoport, Y. Bilik, M. Homyonfer, S. R. Cohen, and R. Tenne, Nature **387**, 791 (1997).
[14]R. H. Wei, C. Rincon, and E. Langa, J. Vac. Sci. Technol. A. **28**, 1126 (2010).
[15]G. Z. Wu and S. L. Ma, Surf. Eng. **26**, 50 (2010).
[16]G. Z. Wu, S. T. Liu, S. L. Ma, K. W. Xu, V. Ji, and P. K. Chu, J. ASTM Int. **8**, 1 (2011).
[17]B. Buecken, G. Leonhardt, R. Wilberg, K. Hoeck, and H. J. Spies, Surf. Coat. Technol. **68–69**, 244 (1994).
[18]J. Valli, U. Makela, and A. Matthews, J. Vac. Sci. Technol. A. **3**, 2411 (1985).
[19]B. Casas, U. Wiklund, S. Hogmark, and L. Llanes, Wear **265**, 490 (2008).
[20]S. J. Bull, and E. G. Berasetegui, Tribology Int. **39**, 99 (2006).
[21]T. Polcar, T. Kubart, R. Novak, L. Kopecky, and P. Siroky, Surf. Coat. Technol. **193**, 192 (2005).
[22]K. Holmberg, and A. Matthews, *Coating Tribology*, edited by Guizhi Wu (Elsevier, Amsterdam, 1994), pp. 41–74.